

Time-Frequency Analysis of Boundary-Layer Instabilities Generated by Freestream Laser Perturbations

Amanda Chou*

NASA Langley Research Center, Hampton, VA, 23681, USA

Steven P. Schneider †

School of Aeronautics & Astronautics, Purdue University, West Lafayette, IN 47907, USA

A controlled disturbance is generated in the freestream of the Boeing/AFOSR Mach-6 Quiet Tunnel (BAM6QT) by focusing a high-powered Nd:YAG laser to create a laser-induced breakdown plasma. The plasma then cools, creating a freestream thermal disturbance that can be used to study receptivity. The freestream disturbance convects downstream in the Mach-6 wind tunnel to interact with a flared cone model. The adverse pressure gradient created by the flare of the model is capable of generating second-mode instability waves that grow large and become nonlinear before experiencing natural transition in quiet flow. The freestream laser perturbation generates a wave packet in the boundary layer at the same frequency as the natural second mode, complicating time-independent analyses of the effect of the laser perturbation. The data show that the laser perturbation creates an instability wave packet that is larger than the natural waves on the sharp flared cone. The wave packet is still difficult to distinguish from the natural instabilities on the blunt flared cone.

Nomenclature

f	frequency, kHz	<i>Subscript</i>
p	pressure, kPa	0 stagnation condition
r_n	nose tip radius, mm	i initial condition
Re/m	freestream unit Reynolds number, m^{-1}	s surface condition
t	time after tunnel starts, s	<i>Superscript</i>
t_p	time after laser pulse is fired, μs	$,$ fluctuation
T	temperature, K	<i>Abbreviations</i>
x	distance from nose tip, mm	FFT fast Fourier transform
θ	azimuthal angle around cone, degrees	RMS root-mean-square
ρ	density, kg/m^3	STFT short-time Fourier transform

I. Introduction

Receptivity, as termed by Morkovin in his 1969 review of transition,¹ is the process by which freestream disturbances enter the boundary layer. When these disturbances enter the boundary layer, they can excite instabilities. These instabilities affect the transition process by growing to create large fluctuations in the boundary layer, which can eventually break down into turbulence.

Receptivity studies can be used to help determine the initial amplitudes of the instabilities. If the receptivity process can be better understood, then a finite-amplitude-based method of transition prediction

*Research Aerospace Engineer, Flow Physics & Control Branch, AIAA Senior Member.

†Professor, AIAA Associate Fellow.

can be developed. Some of the work toward achieving such prediction methods is discussed in Refs. 2 and 3. Amplitude-based prediction methods incorporate more physics than the commonly used empirical and semi-empirical methods. While the empirical and semi-empirical methods work for some cases, many were developed for application to specific geometries or conditions.

Most of the existing studies of high-speed receptivity are computational or theoretical. These studies are typically of planar acoustic waves,^{4,5} vorticity waves,⁶ small thermal disturbances,^{7,8} and particles.⁹ There are some experimental studies in high-speed flow,^{6,10-12} but experiments matching the conditions in the computational and theoretical studies has not been possible. For example, experimental measurements of the effect of particles in a quiet facility would likely damage the highly-polished nozzle and are therefore not feasible. Furthermore, freestream inputs are difficult to characterize through measurement, so the computational and theoretical models of experiments necessarily lack the complete experimental conditions. Thus, computations and theory must estimate these conditions as best as possible to help supplement the experiments. The best understanding of receptivity requires the cooperation of computational, theoretical, and experimental efforts.

A controlled freestream disturbance was created in the Boeing/AFOSR Mach-6 Quiet Tunnel (BAM6QT) at Purdue University to study the receptivity of the boundary layer to a large, discrete thermal disturbance. Similar computations for a very small thermal disturbance were performed by Huang et al.¹³ As in previous studies at Purdue University, this disturbance was generated by focusing a high-powered laser to create laser-induced breakdown of a small region of air.^{11,14,15} Characteristics of this disturbance were measured with pressure sensor probes.¹⁶ The disturbance was eventually allowed to convect downstream to a flared cone model and its effect was measured with several surface-mounted pressure transducers.¹⁷

Previous work showed that the disturbance produced a wave packet.¹⁷ This wave packet convected in the boundary layer at nearly the same speed as the boundary-layer edge velocity. As the wave packet convected downstream, it grew linearly, became nonlinear, and eventually broke down. At similar freestream densities, the wave packet appeared to be much larger on the sharp flared cone than on the blunt flared cone. The wave packet was barely detectable on the blunt flared cone until the last few sensors at the aft end of the cone. On the sharp flared cone, the wave packet appeared to be fairly nonlinear at even the first sensor station.

It was difficult to distinguish the wave packet from the naturally-occurring boundary-layer disturbances, particularly if they were of similar amplitude. Time-frequency analyses are used in this paper to attempt to separate the natural waves from the laser-induced wave packet. Then, an analysis of the changing frequency content over time is used to determine the effect of the freestream disturbance.

II. Facility and Apparatus

A. The Boeing/AFOSR Mach-6 Quiet Tunnel (BAM6QT)

The Boeing/AFOSR Mach-6 Quiet Tunnel (BAM6QT) at Purdue University is a Ludwieg tube that can be run with laminar nozzle-wall boundary layers (Fig. 1). Laminar nozzle-wall boundary layers are required to make the BAM6QT a quiet tunnel and are achieved through the use of several features. The surface of the nozzle is polished to a mirror finish to reduce the likelihood of roughness induced transition. The nozzle is long to reduce the likelihood of transition due to a growing Görtler instability. The air supply is fed through a series of 1- μm particle filters and finally through a 0.1- μm filter to reduce the number and size of particulates in the freestream. A bleed air system also suctions off the air at the nozzle throat to allow for the growth of a new boundary layer on the diverging portion of the nozzle. Typical run times in the tunnel last for about 4 s, although a slight increase in the freestream noise has been observed after about 2 s of run time.¹⁸ A model installed in the tunnel starts at room temperature and remains at the same temperature during these short runs.

B. The Laser Perturber

The laser perturber apparatus creates a perturbation by focusing a high-powered Nd:YAG laser to a small volume in the freestream of a wind tunnel. An Nd:YAG laser equipped with enhanced spatial mode and an injection seeder is used in this apparatus. The maximum energy per pulse is typically around 250 mJ for a 7-ns pulse at 10 Hz. The perturbation-forming optics consist of three air-spaced achromatic triplets for YAG wavelengths. An ionized plasma is created at the focus of this lens system via laser-induced breakdown.

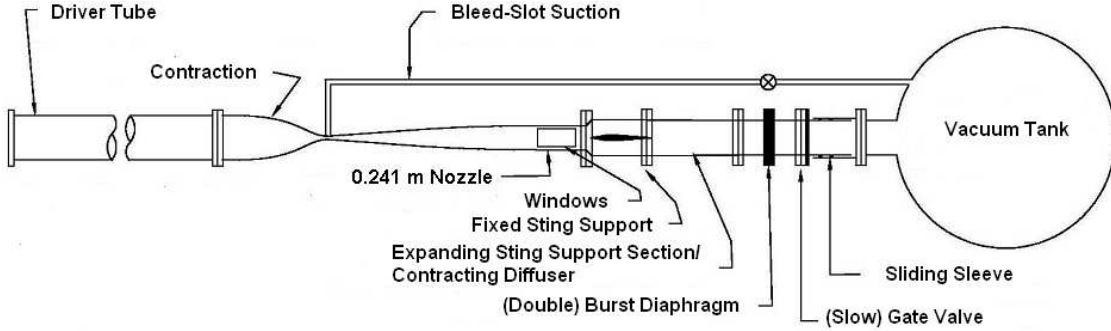


Figure 1. A schematic of the Boeing/AFOSR Mach-6 Quiet Tunnel.

This plasma cools and a weak shock emanates from the thermal core, but quickly decays. The thermal perturbation is used as a controlled disturbance and allowed to convect downstream to interact with a test body, as shown in Fig. 2.

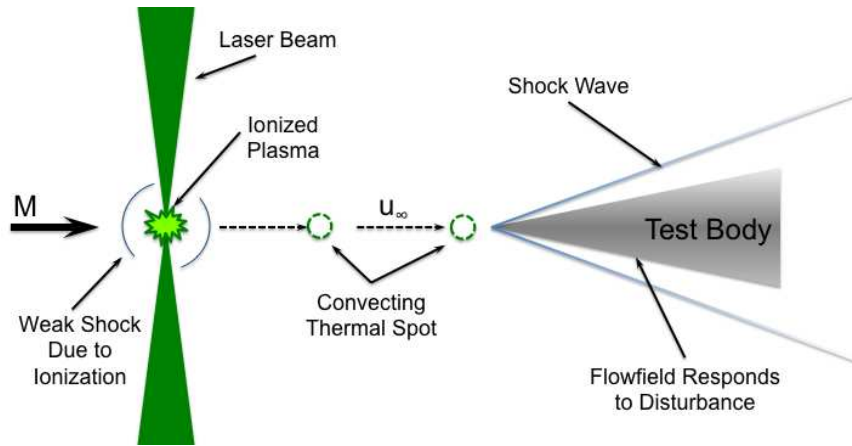


Figure 2. A schematic of the laser perturbation placed upstream of a model in a wind tunnel.

III. Model

The model used for this experiment was a flared cone. This model was designed by Wheaton and Juliano to have large second-mode waves, as discussed in Ref. 19. The geometry of this model is defined as a body of revolution bounded by a circular arc with a 3-meter radius. A photograph of the flared cone is shown in Fig. 3. Two nosetips are available for this model: a 1-mm-radius (blunt) nosetip and a 0.16-mm-radius (sharp) nosetip. The nosetips are nearly hemispherical and the curvature of the nosetip lies tangent to the circular-arc flare. The different nosetips have different lengths. Thus, the sensor locations will change relative to the nosetip, depending on the nosetip used. Previous measurements without the freestream laser perturbation for the blunt nosetip model are available in Ref. 19 and similar measurements with the sharp nosetip model are available in Ref. 20.

A total of fourteen PCB 132A31 fast pressure transducers were installed in the cone. Eight of these piezoelectric pressure transducers were installed along the 0° ray, which faced 180° away from the incoming Nd:YAG laser beam. Three sensors were installed on each of the other two axial sensor rays at $+120^\circ$ and -120° . The sensors were sampled at 2 MHz for the entire run. These data were recorded with three digital phosphor oscilloscopes, which can read and record four different channels. These oscilloscopes each have a maximum record length of 250 million points. Two have an analog bandwidth of 500 MHz and one has an analog bandwidth of 1 GHz. Due to the limitation in the number of long-memory oscilloscopes, only a total

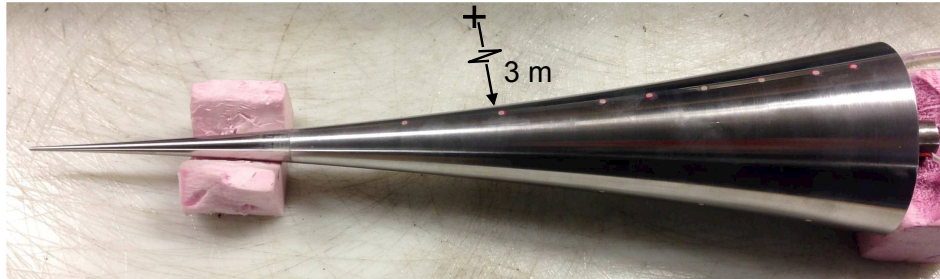


Figure 3. A photograph of the 3-m-circular-arc flared cone and PCB sensors.

of 12 of the pressure transducers could be monitored in any given run.

IV. Analysis

The pressure gradient on the flared cone produces naturally large second-mode waves.^{19,20} The freestream laser-generated disturbance generates a wave packet in the boundary layer of the flared cone of the same frequency as the natural second mode.¹⁷ The analysis of the perturbation's effect on the flared cone boundary layer is dependent upon the window of samples used. A time-frequency analysis of the data can be performed to determine the transient effect of the perturbation. This form of analysis can depict the change of the frequency content of the data over time.

This paper will compare different conditions for each of the two nosetips. Reference 17 showed that when the conditions for the sharp and blunt nosetip are matched, breakdown of the wave packet occurs on the sharp nosetip while very little growth of the wave packet on the blunt nosetip is observed. In fact, the wave packet on the sharp nosetip was already fairly nonlinear by the time the disturbance reached the first measurement station. Thus, the linear growth of the wave packet was not observed on the sharp flared cone and an estimate of the initial amplitude of the wave packet was not possible on the sharp flared cone. In order to better investigate the growth of the wave packet on each cone, two different test conditions were chosen, one for each nosetip. The condition for the blunt nosetip measurements was at a higher Reynolds number than the condition for the sharp nosetip measurements. These conditions were chosen so that more of the growth process of the wave packet could be better observed on each of the cones. At a lower Reynolds number, more linear growth can be captured on the sharp flared cone. At a higher Reynolds number, more nonlinear growth can be captured on the blunt flared cone.

Since the wave packet generated by a laser perturbation contains the same frequency content as the natural waves, it becomes difficult to distinguish between the two when both are of similar amplitude. The time-frequency analysis aids in distinguishing when the laser-generated disturbance passes by a single sensor. The frequency content of the perturbation over time can be analyzed by using time-frequency methods such as the short-time Fourier transform or a wavelet transform. A general uncertainty principle exists for time-frequency analyses, where resolution of the frequency content will provide poorer resolution of the signal over time, and vice versa. Generally, the short-time Fourier transforms will have better frequency resolution and poorer time resolution. On the other hand, wavelet transforms will have better time resolution and poorer frequency resolution.

A. Power Spectra and Root-Mean-Square

The power spectra shown in this paper are computed by taking a fast Fourier transform (FFT) of a 1000-point window at some interval of time between laser perturbations. A Blackman windowing function is applied to the 1000-point window and the FFTs are computed using the Welch spectrum estimation method. The FFTs from 10 different laser shots are ensemble averaged together to form the power spectra. Previous analysis in Ref. 17 has shown that the FFTs do not change much during the duration of the run.

The RMS amplitudes of the second mode were calculated by integrating the spectra in a 4-kHz frequency band centered around the indicated frequency, and then taking the square root. The mean flow and the linear stability of the second-mode frequencies were computed using the formulation described in Ref. 21. Two-dimensional unsteady compressible Navier-Stokes equations written in cylindrical coordinates

are solved using a 5th-order weighted essentially non-oscillatory (WENO) scheme for space discretization and a 3rd-order total-variation-diminishing (TVD) Runge-Kutta scheme for time integration. The stability computations use linear stability theory. The measured RMS amplitudes were compared to the computations at the most amplified second-mode frequency band for the conditions given.

The N -factor is defined as:

$$N = \ln \frac{A}{A_0} \quad (1)$$

where A is the amplitude of the instability at a given location and A_0 is the initial instability amplitude. The RMS amplitudes are normalized by the calculated RMS amplitude at the first sensor location because the initial amplitude is unknown. The relationship between this normalized RMS amplitude (A/A_1) and the N -factor is given by

$$N = \ln \left(\frac{A}{A_1} \frac{A_1}{A_0} \right) = \ln \frac{A}{A_1} + \ln \frac{A_1}{A_0} \quad (2)$$

where A_1 is the RMS amplitude at the first sensor station. The natural logarithm of the normalized RMS amplitude will be the same scale as the N -factor with some offset defined by the N -factor at the first sensor station where linear growth is observed. Subsequent plots containing RMS information will have the natural log of the normalized RMS and an appropriate offset so that the measured data can be plotted to compare to the computations. In these comparisons, the computations were performed at the same conditions as the experiment. The grids used for the sharp flared cone and the blunt flared cone were about 6000 points in the streamwise direction and up to 500 points in the wall-normal direction.

B. Short-Time Fourier Transform Analysis

The short-time Fourier transform (STFT) is taken by sliding a window over different portions of the time data and then taking the FFT of the data in the given window. The frequency content can then be mapped for a given time window and visualized as a spectrogram. This is essentially a contour plot of the FFTs at each time window. In the cases shown here, each STFT is computed using 600-point (0.3-ms) Blackman windows with a 95% overlap. The frequency is given on the vertical axis, and the time after the laser pulse is fired is given on the horizontal axis. This method of analysis is known for providing better resolution in the frequency domain than in the time domain.

C. Continuous Wavelet Transform Analysis

A continuous wavelet transform was used to determine changes in frequency over time. Wavelet transforms allow for the usage of windowing with variable-sized regions, unlike the STFT, which uses a fixed window over time. Using the algorithm outlined by Jordan et al.,²² a complex Morlet wavelet transform was applied to the time response measured at each sensor station for a single laser shot. This wavelet transform is expressed as

$$W(a, \tau) = \int_{-\infty}^{\infty} f(t) \psi_{a, \tau}^*(t) dt \quad (3)$$

The Morlet wavelet is a complex exponential multiplied by a Gaussian window and expressed in the time domain as

$$\psi(t) = \exp(i\omega_\psi t) \exp(-|t|^2/2) \quad (4)$$

where $\omega_\psi = 5.5$ was the constant used to satisfy the admissibility condition. This admissibility condition ensures that once a function is transformed to the wavelet domain, it can be recovered by applying the inverse wavelet transform. The dilations of the mother wavelet (Equation 4) are given by

$$\psi_{a, \tau} = a^{-1/2} \psi \left(\frac{t - \tau}{a} \right) \quad (5)$$

where $a^{-1/2}$ is a normalization that gives all dilated versions of Equation 4 the same energy and τ is a shifting property of the transform. The frequency content of the Morlet wavelet transform is expressed here as the magnitude of the wavelet transform in the following plots.

V. Wave Packet Development on the Sharp Flared Cone

Figure 4 shows the time response to one laser shot at each sensor location. Each plot shows the unfiltered time response as well as several bandpass-filtered time responses. These filtered time traces are plotted with an arbitrary offset from the unfiltered time response. The first band is between 11–130 kHz, which corresponds to either the expected frequency band of the first mode or the subharmonic of the natural second mode. The second band is between 130–300 kHz, which corresponds to the expected frequency range of the natural second mode. The third band is between 300–580 kHz, which corresponds to the first harmonic of the second mode.

The wave packets at each station appear to consist of multiple “bursts,” where the envelope of the wave packet has multiple maxima. This is most notable starting at the first sensor station of $x = 230.5$ mm, where the wave packet appears to consist of two bursts. At $x = 230.5$ mm, the frequency content of the wave packet appears to consist mostly of the second-mode frequencies. At farther downstream stations, the first harmonic of the second mode appears when the wave packet passes. Finally, at $x = 408.6$ mm and farther downstream, there appears to be some increase in the lower frequency band. Previous power spectra in Ref. 15 suggests that this may be the same location where breakdown begins to occur.

Figure 5 shows the STFT of the measured response of the boundary layer to a wave packet generated by a freestream laser perturbation. Each sub-figure shows the change in the frequency content over time at the indicated sensor station. The frequency is given by the vertical axes, the time after a laser pulse is given by the horizontal axes, and the power of the pressure fluctuations is given by the color bar on the right. Prior to the passage of the wave packet, before $t_p = 0.4$ ms at all stations, the frequency content shows low background noise, with a peak at the expected second-mode frequency of about 227 kHz. The presence of this peak is due to the natural second-mode wave, which is fairly large on this model.²⁰ When the wave packet arrives at a sensor, the power in the second-mode frequency rises and broadens in bandwidth. As expected, the wave packet takes longer to arrive as the distance between the sensor and the nosetip increases. After the wave packet has passed, the frequency content resembles the content prior to the passage of the wave packet. This shows that the wave packet has a transient effect.

At the most upstream location of $x = 230.5$ mm (Fig. 5(a)), there is a peak in power near 85 kHz. The power in the low frequency band of 11–130 kHz is comparatively lower between $x = 280.9$ mm and $x = 381.6$ mm. Previous analysis has shown that breakdown of the wave packet starts to occur near $x = 381.6$ mm, which explains the increase in power at the lower frequencies at the aft end of the cone. The peak in power near 85 kHz at $x = 230.5$ mm is present before and after the passage of the wave packet, indicating that this instability is not related to the presence of the freestream laser perturbation. In fact, a lower-frequency peak at this sensor station has been observed previously in Ref. 20, where no laser perturbation was placed upstream of the model. The cause of this peak is as of yet unknown.

At farther downstream locations (Figs. 5(b)–5(g)), the presence of a harmonic appears around the same time as the wave packet. The harmonic of the second mode occurs only when the wave packet passes over the sensor, indicating that the freestream laser perturbation creates a nonlinear disturbance in the boundary layer while the natural freestream disturbances at this condition do not. Finally, evidence of breakdown of the wave packet is observed from $x = 408.6$ –450.5 mm (Figs. 5(f)–5(h)). At these sensor locations, the broadband frequency content begins to increase in power when the wave packet passes over the sensor. These characteristics show that the freestream laser perturbation creates a temporary increase in the boundary-layer disturbance level, and that its effect is transient.

The transient effect of the laser-generated perturbation can also be visualized using a comparison of the power spectra at different times after the laser pulse is fired. Power spectra taken prior to when a laser shot is fired are compared to power spectra with windows after a laser shot is fired in Fig. 6. The FFT windows after the laser shot is fired are centered around the expected arrival time of the wave packet. The electronic noise at each sensor station is given by the dotted black lines. The power spectrum over a 1000-point window just prior to when a laser shot is fired ($t_p = -3.0$ to -2.5 ms) is shown by the dot-dashed blue lines. The power spectrum over a 1000-point window including the wave packet is shown by the solid red lines.

The shape of the spectra in Fig. 6 indicate that without the presence of the wave packet, the harmonics of the second mode do not develop along the length of the cone. Thus, the natural second-mode instabilities remain fairly linear along the length of the cone at the tested condition. The shape of the spectra when FFTs are taken over the wave packet indicate that the wave packet has the same frequency content as the natural second mode. The wave packet becomes nonlinear by $x = 280.9$ mm, as indicated by the presence of higher harmonics in the power spectrum. The wave packet then starts to break down by $x = 408.6$ mm,

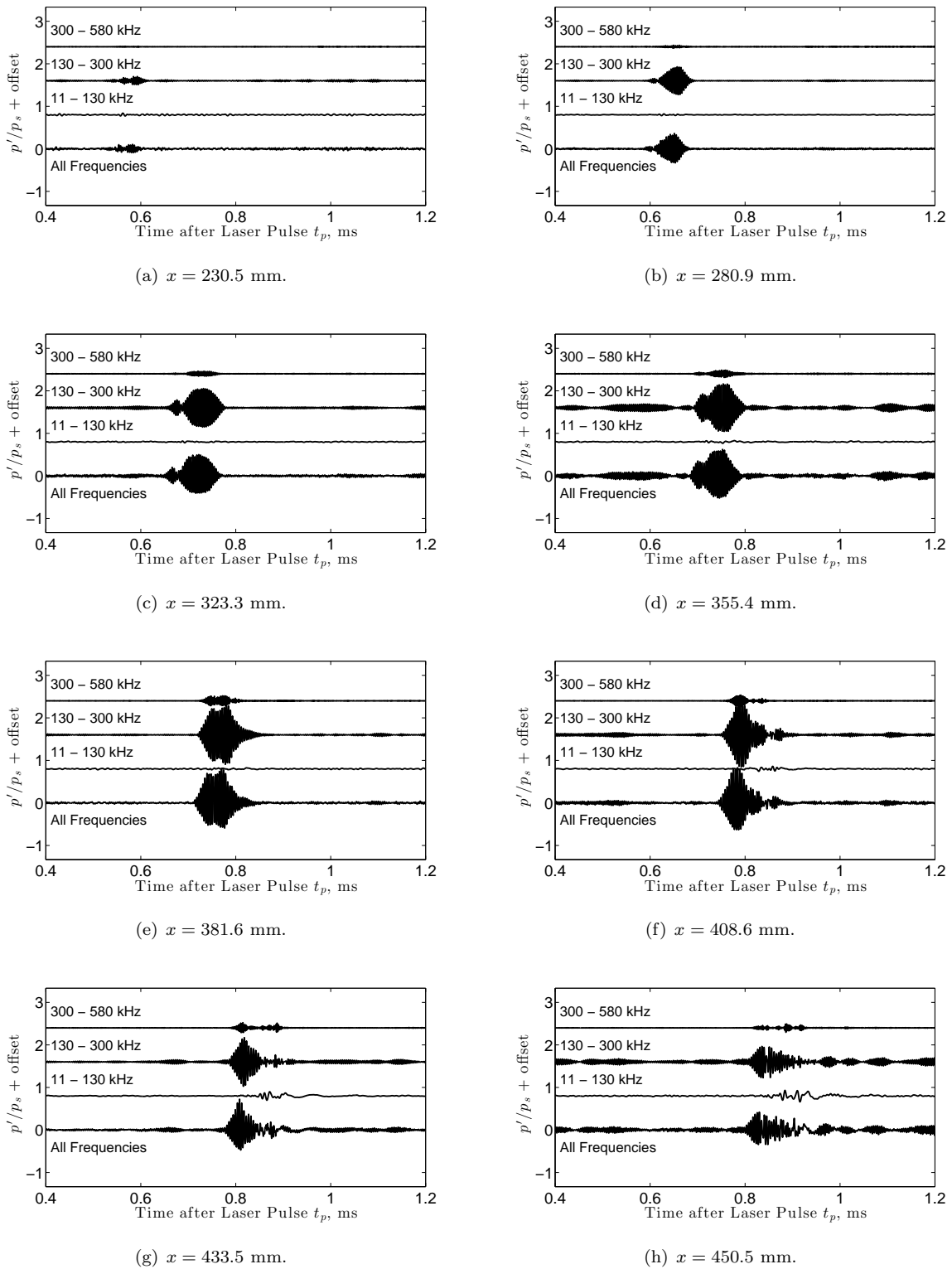


Figure 4. Filtered time traces showing the axial development of a laser-generated wave packet in the boundary layer of a sharp flared cone: $r_n = 0.16$ mm, $p_0 = 534.3$ kPa, $T_0 = 428.3$ K, $\rho_\infty = 0.022$ kg/m³, $Re/m = 5.81 \times 10^6$ /m.

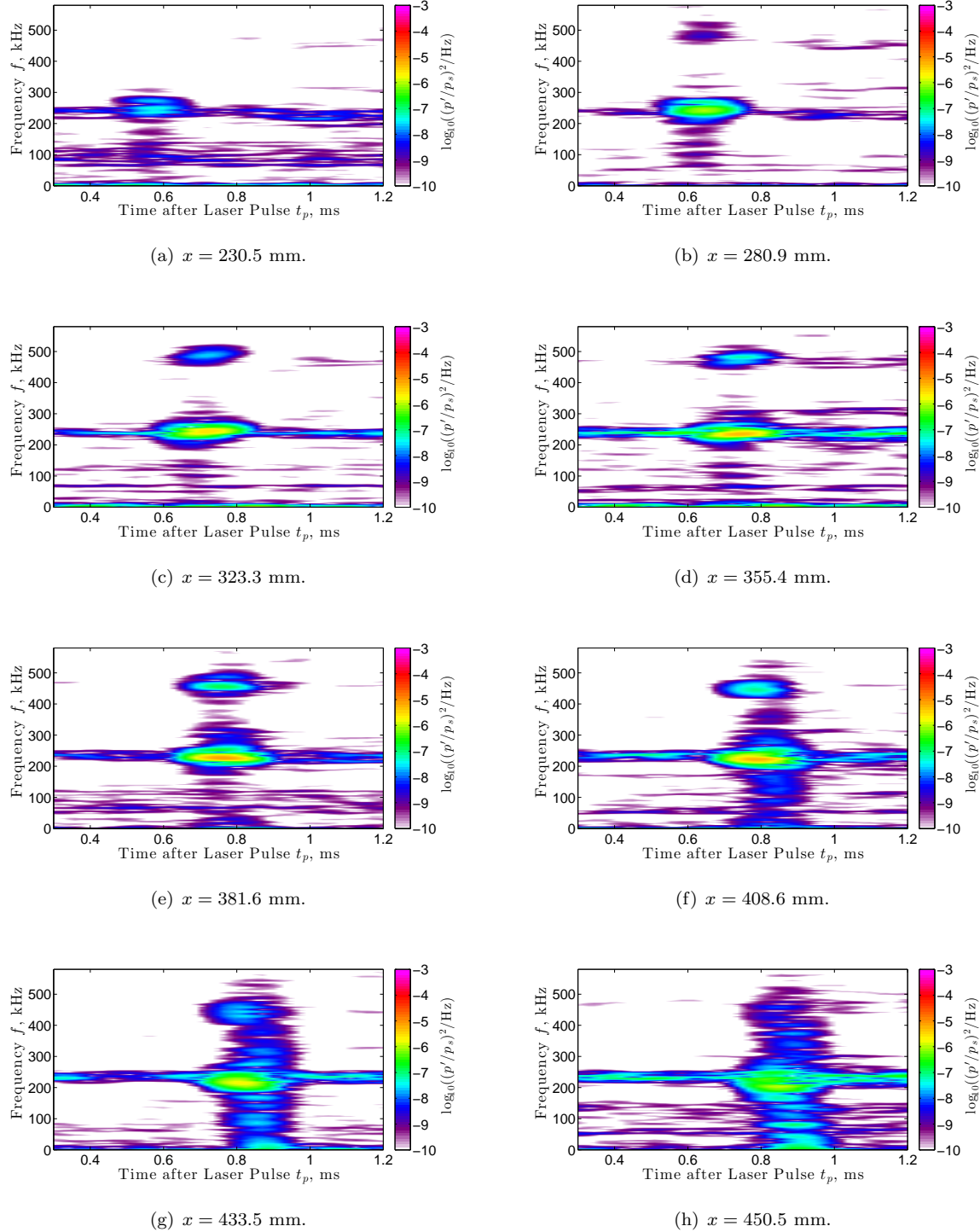


Figure 5. Short-time Fourier transforms showing the axial development of a laser-generated wave packet in the boundary layer of a sharp flared cone: $r_n = 0.16$ mm, $p_0 = 534.3$ kPa, $T_0 = 428.3$ K, $\rho_\infty = 0.022$ kg/m³, $Re/m = 5.81 \times 10^6/\text{m}$.

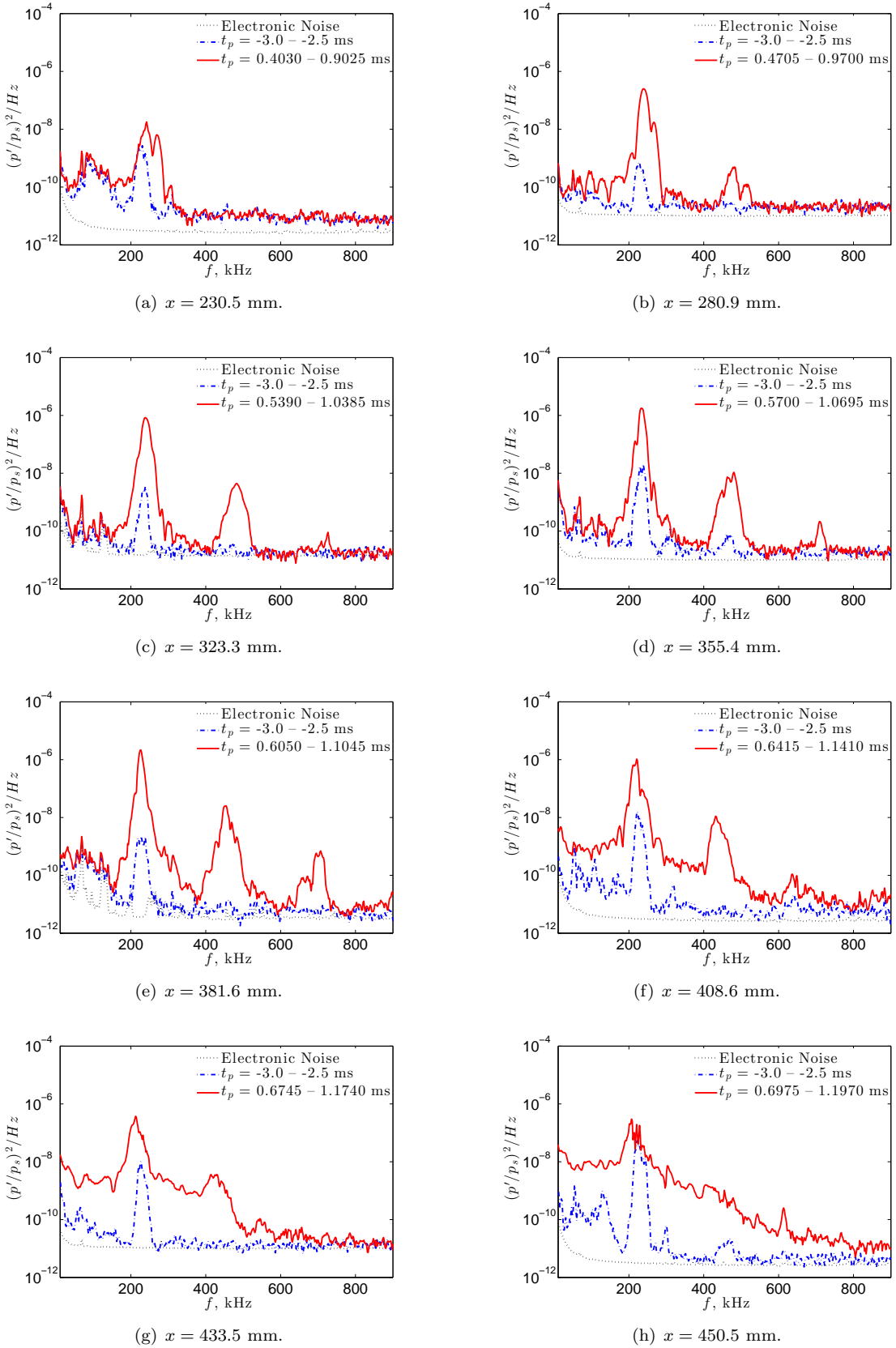


Figure 6. Comparison of FFTs taken prior to a laser shot (blue) and over a wave packet (red) at each axial sensor station: $r_n = 0.16$ mm, $p_0 = 534.3$ kPa, $T_0 = 428.3$ K, $\rho_\infty = 0.022$ kg/m³, $Re/m = 5.81 \times 10^6$ /m.

as indicated by the presence of spectral broadening, and is fairly turbulent by the last sensor station of $x = 450.5$ mm.

The growth of the instabilities within the second-mode frequency band is distinctly different when the wave packet is present than when it is not present. A comparison of the computations and measurements of the growth of the second-mode peak at different frequencies is given in Fig. 7. Three cases are compared here: when the FFTs used for computing the spectra are taken over a window with no wave packet (open circles), when the FFTs used for computing the spectra are taken over a window with the wave packet (solid squares), and for spectra computed for a separate tunnel run without the laser perturber (open triangles). The growth of the second-mode waves appear to match the computations fairly well when a wave packet is present in the time traces up until the point where breakdown of the wave packet is observed in the FFTs. Breakdown is taken to be the point at which the spectral content of the wave packet begins to broaden. When no wave packet is present, however, the second-mode waves often do not appear to grow much at all and there is increased scatter in the measured RMS. The measurements of the second mode are smaller in amplitude without the presence of the freestream laser perturbation, thus, the lack of resolution in the measurement may be enough to create the scatter observed.

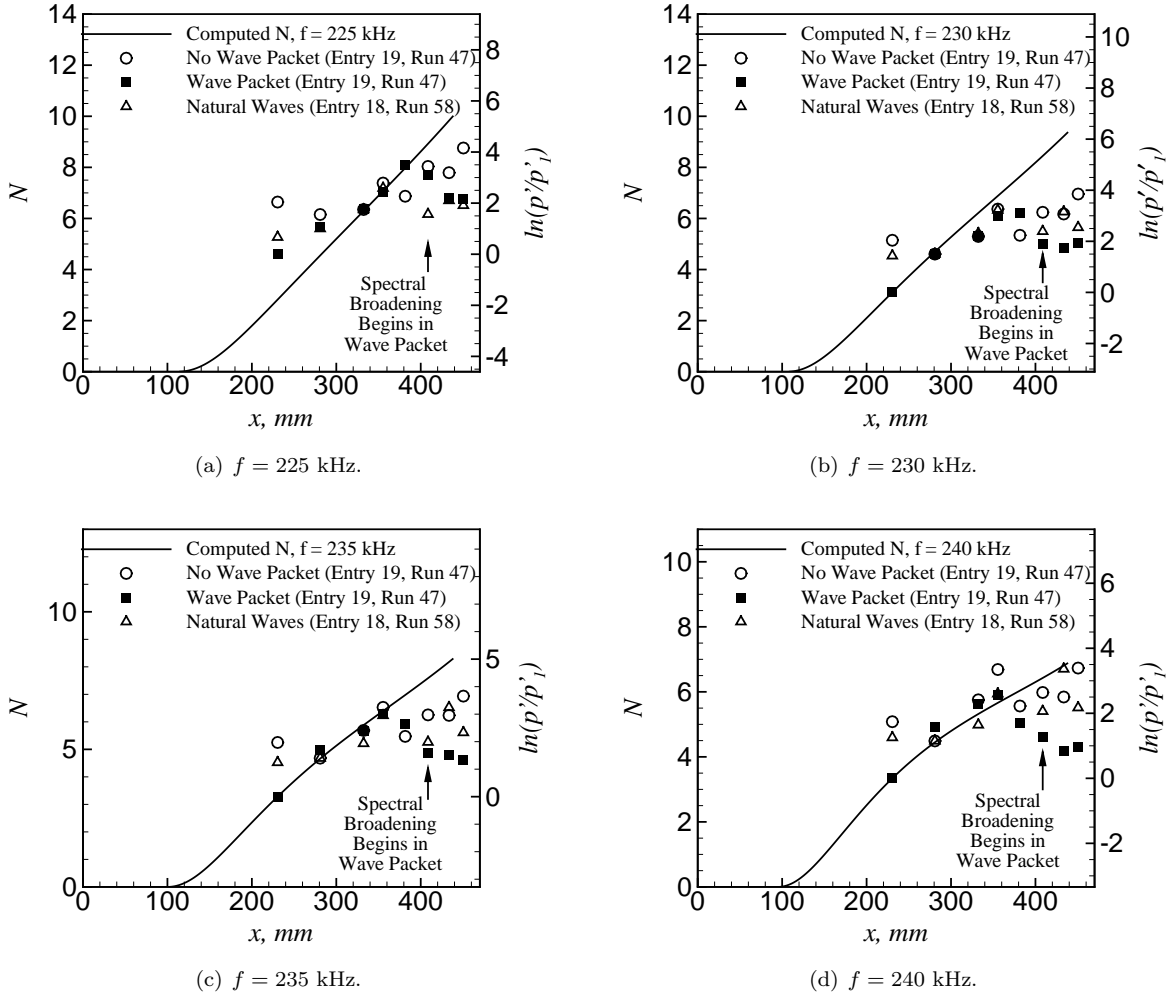


Figure 7. Comparison of normalized measured RMS pressure at each sensor station on the sharp flared cone to the computed N factor: $r_n = 0.16$ mm, $p_0 = 534.3$ kPa, $T_0 = 428.3$ K, $\rho_\infty = 0.022$ kg/m³, $Re/m = 5.81 \times 10^6$ /m.

The computed RMS amplitudes of the second mode across the entire second mode frequency peak are given in Table 1. The first column tabulates the RMS amplitudes normalized by the surface pressure at each sensor station, p'/p_s . The surface pressure along the flared cone is not constant due to a pressure gradient imposed by the geometry of the model. Thus, the second column in Table 1 shows the RMS amplitudes normalized by the freestream static pressure (p'/p_∞), which is constant regardless of the sensor station. The

spectral broadening in Fig. 6(f) indicates that the packet is starting to break down near $x = 408.6$ mm. The RMS amplitude at this location on the sharp flared cone is 12.4%, which is similar to the amplitudes at breakdown seen by Marineau in Ref. 3 on a 7-degree straight cone. However, the maximum amplitude of the wave packet only reaches about 16% on the sharp flared cone, which is almost half of what is observed by Marineau on the 7-degree cone. An estimate of the initial amplitude of the perturbation at the neutral point on the flared cone at this condition yields about $2.1 \times 10^{-5} p_\infty$.

Table 1. Table of measured RMS amplitudes of the second-mode frequency peak on a sharp flared cone.

Axial Position x , mm	Normalized RMS Pressure p'/p_s 150–350 kHz	Normalized RMS Pressure p'/p_∞ 150–350 kHz
230.5	2.05	0.176
280.9	7.31	0.704
332.3	13.4	1.45
355.4	16.3	1.87
381.6	16.2	1.97
408.6	12.4	1.60
433.5	8.21	1.13
450.5	7.57	1.08

While the STFT can provide higher-resolution information on the frequency content, the time resolution of the spectrogram is fairly poor. Wavelet transforms can provide higher-resolution information in the time domain, but provide fairly poor-resolution information about the frequency content. The Morlet wavelet transform is applied over the same laser shot as in Figs. 4 and 5 and the magnitude of the transform is mapped in Fig. 8. The axes here remain the same as in the STFT spectrograms, but the color contours now correspond with the magnitude of the wavelet transform coefficient. The wave packets are more clearly distinguished from the natural waves in the wavelet transforms in Fig. 8 than in the STFT in Fig. 5. In fact, the features of the double burst seen in Figures 4(c)–4(e) appear more clearly in Figs. 8(c)–8(e), respectively. Similar double burst features have been observed in computations of nonlinear wave packets in Refs. 23 and 24. The naturally-occurring second-mode disturbances are also visible in the wavelet transform as smaller-amplitude bursts that occur before and after the wave packet. These naturally-occurring disturbances are amplitude-modulated in time. These distinct features of amplitude modulation were not observed previously in the STFTs for the naturally-occurring disturbances. Thus, if the natural disturbances are large, the amplitude modulation seen in the natural disturbances can be mistaken as wave packets, when using a simple thresholding method with wavelet analysis to pick out wave packets.

VI. Wave Packet Development on the Blunt Flared Cone

Similar analysis can be applied to measurements on the blunt flared cone. Figure 9 shows the measurements from the surface-mounted pressure transducers for one laser shot. Each plot in Fig. 9 shows the unfiltered trace along with traces that have been band-pass filtered at the indicated frequencies. Again, the filtered time traces are offset from the unfiltered time trace by an arbitrary amount. There is a slight increase in the signal of the second-mode frequency band. The increase in signal appears in Figs. 9(a)–9(d) at the same time: $t_p \approx 0.85$ ms. The arrival time of the slight signal increase does not appear to change with the sensor distance from the nosetip. Thus, it does not appear to convect like the wave packet. The cause of this signal increase is not clear, but is repeatable for every laser shot ahead of the blunt flared cone for every tested Reynolds number. The wave packet does not appear to be detectable until $x = 351.1$ mm. Then, the wave packet grows and develops harmonics at $x = 378.1$ mm. These harmonics also grow as the distance between the nosetip and sensor increases. At these test conditions, the wave packet does not appear to break down.

The STFTs of the data from the sensors on the blunt flared cone are plotted as spectrograms in Fig. 10. These STFTs contain similar information to the filtered time traces shown in Fig. 9. Again, there appears to be a slight increase in pressure fluctuations at the second-mode and harmonic frequencies starting at the

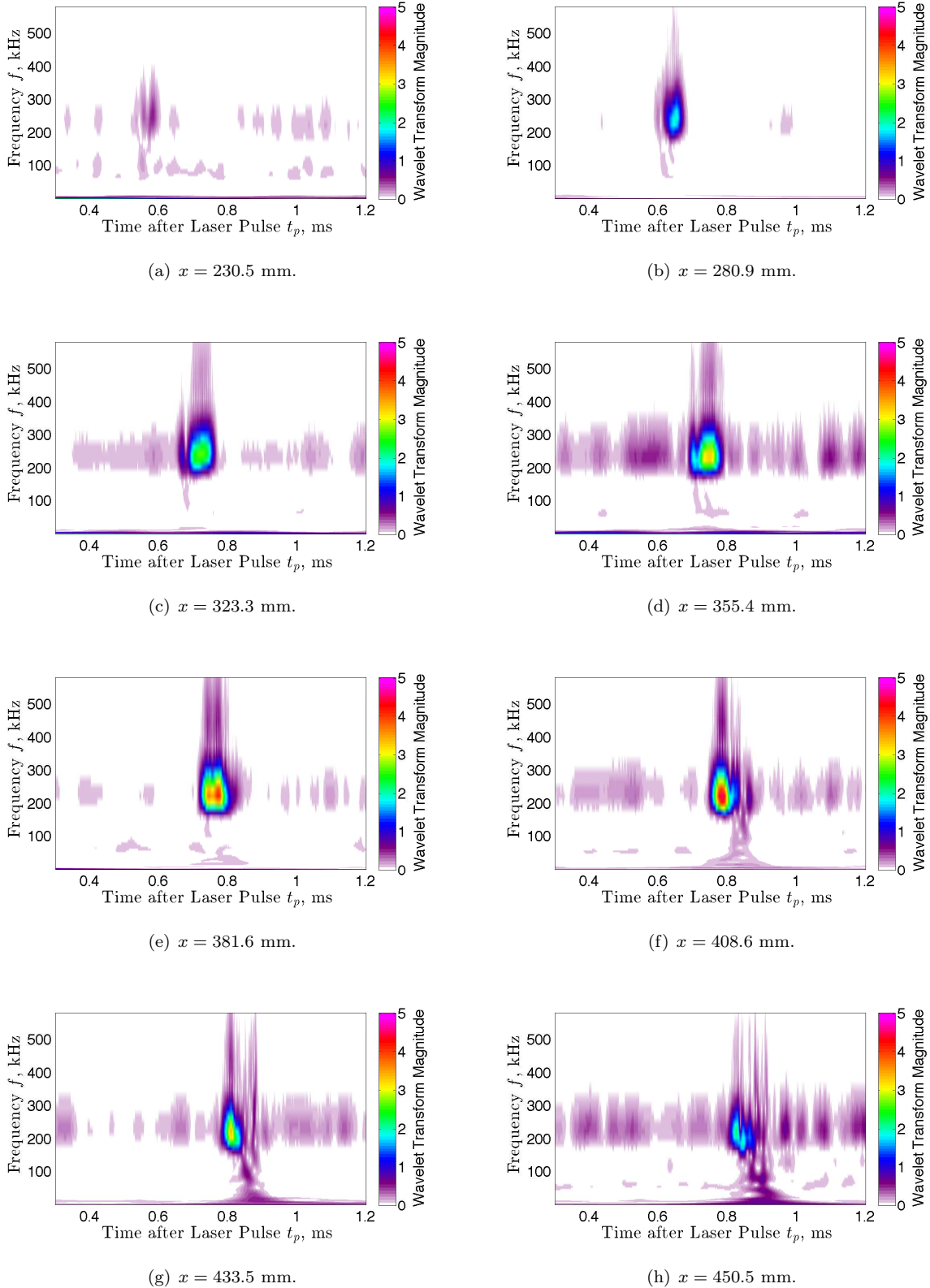


Figure 8. Morlet wavelet transforms showing the axial development of a laser-generated wave packet in the boundary layer of a sharp flared cone: $r_n = 0.16$ mm, $p_0 = 534.3$ kPa, $T_0 = 428.3$ K, $\rho_\infty = 0.022$ kg/m³, $Re/m = 5.81 \times 10^6$ /m.

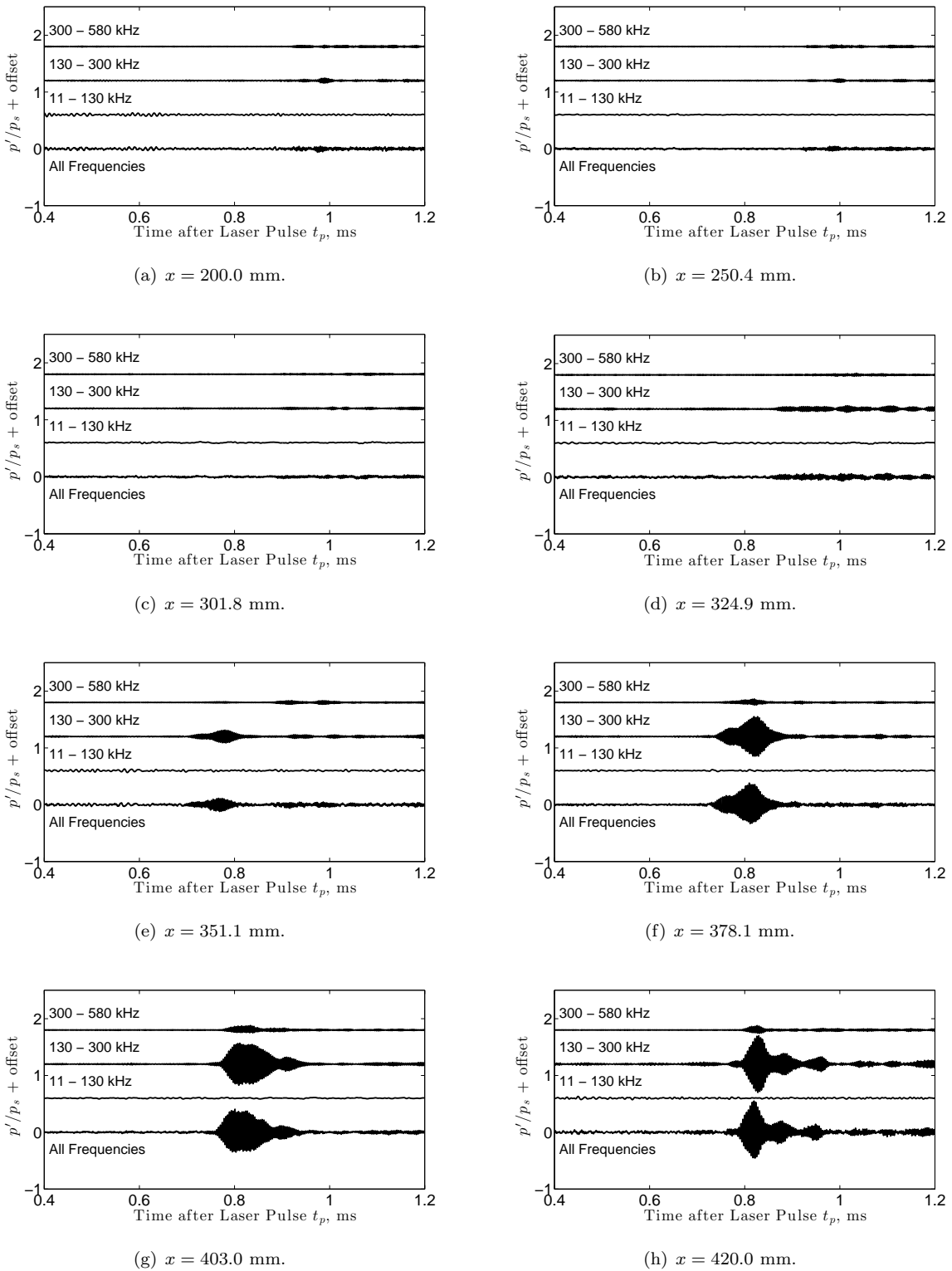


Figure 9. Filtered time traces showing the axial development of a laser-generated wave packet in the boundary layer of a blunt flared cone: $r_n = 1$ mm, $p_0 = 769.1$ kPa, $T_0 = 433.7$ K, $\rho_\infty = 0.032$ kg/m³, $Re/m = 8.22 \times 10^6$ /m.

same time ($t_p = 0.85$ ms) at several locations. The increase in amplitude is not present prior to each laser shot, as shown in Fig. 11.

The arrival of the wave packet is not detectable until it reaches $x = 351.1$ mm, when the power in the second-mode frequency band is 1.5 orders of magnitude greater than the unknown signal increase. When the wave packet is detected at $x = 351.1$ mm (Fig. 10(e)), it arrives almost 0.25 ms prior to the unknown signal increase. At this sensor station, the increase in the harmonic frequency band does not appear to start until around 0.8 ms, so it may not be related to the presence of the wave packet. Between $x = 378.1$ mm and $x = 420.0$ mm, the second-mode frequency band and the harmonic frequency band both show an increase in power at the same time, indicating that the wave packet is probably nonlinear at these stations. Spectral broadening does not appear to occur at this condition for the blunt flared cone.

A comparison of the power spectra using windows centered both on (red line) and off (blue line) of the wave packet is shown in Fig. 12. The power spectra are fairly similar when comparing FFT windows taken prior to a laser shot and centered over a time period when the wave packet is expected to arrive, between $x = 200.0$ mm and $x = 301.8$ mm (Figs. 12(a)–12(c)). This shows a slightly different picture compared to the STFTs. A majority of the 1000-point windows do not include much of the unknown signal increase at $t_p = 0.85$ ms for these first few sensor stations. Thus, the contribution of the unknown signal increase to the spectrum estimate is small. Note that there is also a low-frequency peak at $x = 200.0$ mm centered at about 91 kHz. This peak is similar to the low-frequency peak seen at the first sensor station on the sharp cone in that it does not appear at the other sensor stations. This peak is present in both spectra shown in Fig. 12(a), so it is probably unrelated to the passage of the wave packet. The presence of a freestream laser perturbation does not appear to have a measurable effect at these most upstream sensor stations.

The power spectra at $x = 324.9$ mm show that there is a slight increase in power in the second-mode frequencies and a possible first harmonic when the FFT window is centered about the wave packet. When the FFT window is centered around a time period before a laser pulse is fired, there does not appear to be a first harmonic of the second mode in the power spectrum. At farther downstream stations (Figs. 12(d)–12(h)), the second mode and its first harmonic grow when the FFT window is centered about the wave packet. Again, when the FFT window is centered about a time period before the laser pulse is fired, there does not appear to be a first harmonic of the second mode in the power spectra. These spectra show that the freestream laser perturbation increases the second-mode amplitude temporarily and causes the disturbances to grow larger than if only the natural disturbances were present. Unlike on the sharp cone, the wave packet on the blunt flared cone does not appear to experience spectral broadening. Thus, the measurements suggest that the wave packet on the blunt flared cone does not break down by the time it arrives at the last sensor station.

The normalized RMS amplitudes of the measurements are compared to the computations in Fig. 13. As on the sharp flared cone, it appears that when the freestream perturbation is present, linear growth of the perturbation is clear and follows the computations fairly closely. However, when the perturbation is not present, the RMS amplitudes are relatively similar at each of the sensor stations, with some scatter. It is possible that without the presence of the laser perturbation, the freestream disturbances create boundary-layer instabilities that are very small, resulting in low signal-to-noise ratios. Consequently, the relative differences between these smaller instabilities may not be as apparent as when the amplitudes are larger.

The computed RMS amplitudes of the second mode across the entire second mode frequency peak is given in Table 2. No spectral broadening was observed on the blunt flared cone, so the RMS amplitude of the wave packet at transition is unknown. The maximum amplitude of the wave packet again reaches about 16% on the blunt flared cone. However, the location of the maximum amplitude of the wave packet is at the end of the measurement range, so it is unknown if the wave packet continues growing. The estimated initial amplitude of the second mode at the neutral point of the blunt flared cone is estimated to be about $8.0 \times 10^{-7} p_\infty$ at this condition. This initial amplitude is almost two orders of magnitude less than on the sharp cone, despite that the freestream unit Reynolds number analyzed here is 40% higher than the freestream unit Reynolds number on the sharp cone. Reference¹⁶ showed that as the freestream unit Reynolds number increases, the amplitude of the freestream laser perturbation should also increase. Thus, the blunt flared cone should be subjected to a larger-amplitude freestream disturbance than the sharp flared cone in these analyses. However, the estimate of the initial disturbance on the blunt flared cone is still much smaller than on the sharp flared cone, indicating the receptivity of the blunt flared cone to the laser perturbation is much smaller than the receptivity of the sharp flared cone.

The Morlet wavelet transforms for measurements on the sharp flared cone revealed the wave packets at

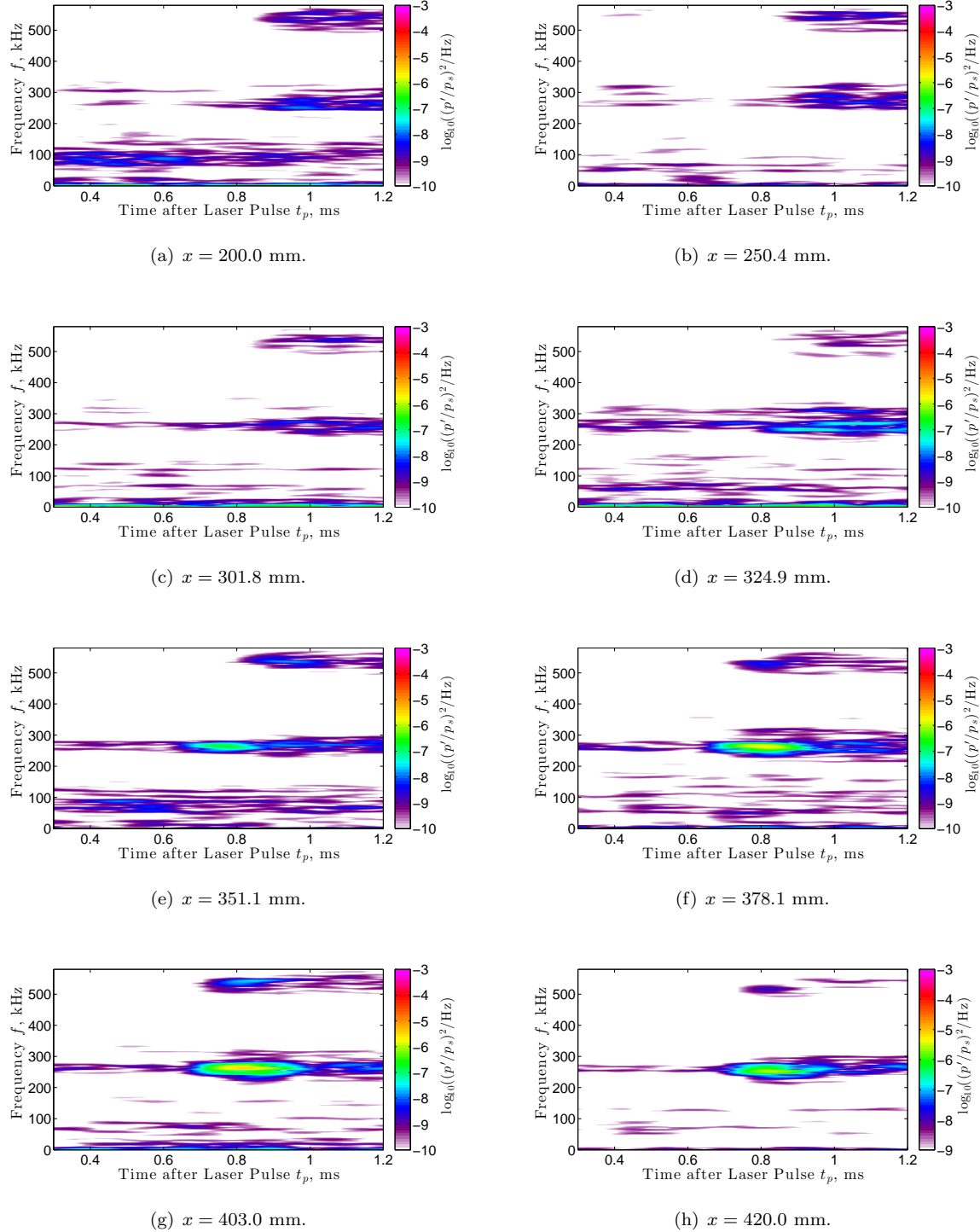


Figure 10. Short-time Fourier transforms showing the axial development of a laser-generated wave packet in the boundary layer of a blunt flared cone: $r_n = 1$ mm, $p_0 = 769.1$ kPa, $T_0 = 433.7$ K, $\rho_\infty = 0.032$ kg/m³, $Re/m = 8.22 \times 10^6$ /m.

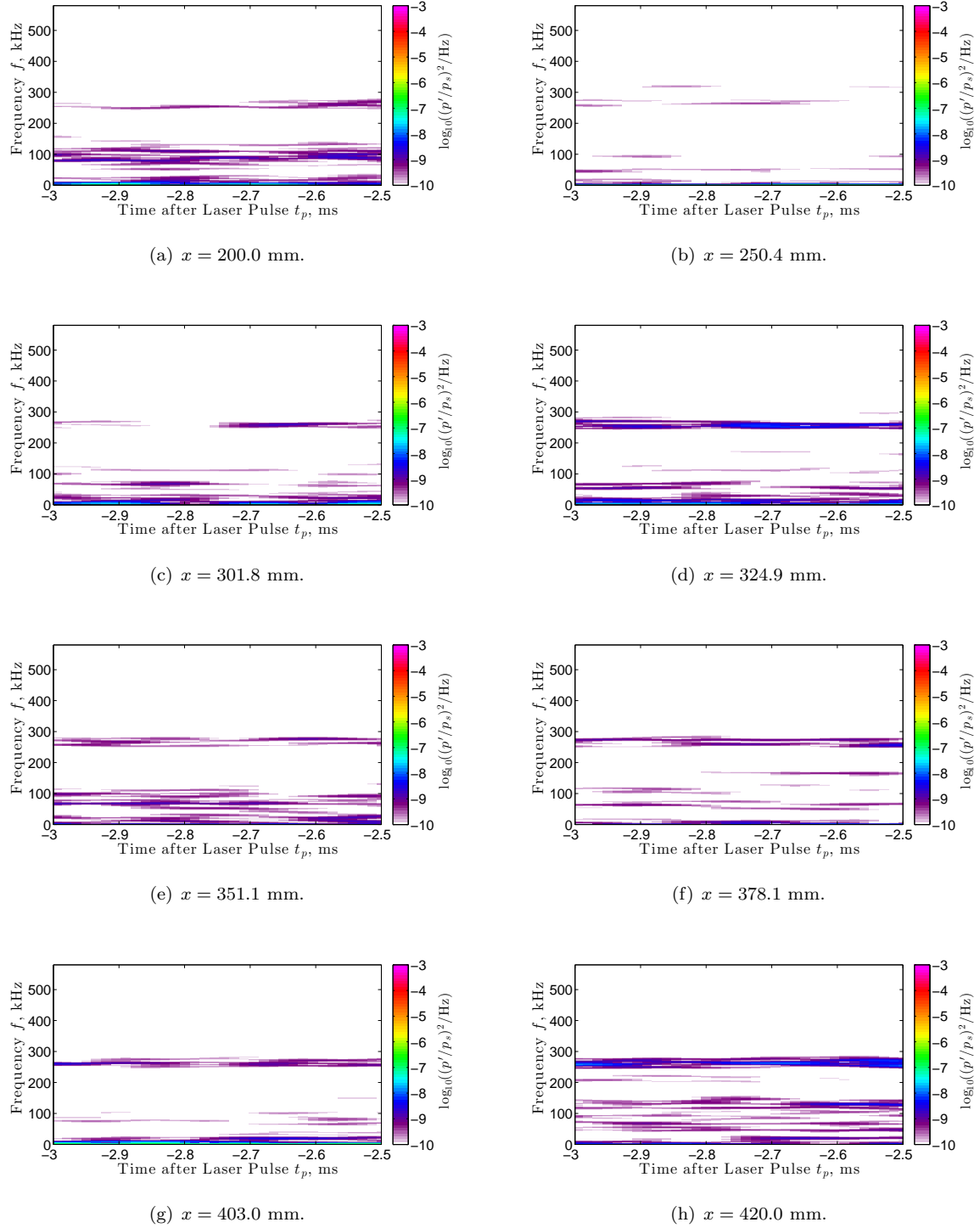


Figure 11. Short-time Fourier transforms of measurements from before the laser shot: $r_n = 1$ mm, $p_0 = 769.1$ kPa, $T_0 = 433.7$ K, $\rho_\infty = 0.032$ kg/m³, $Re/m = 8.22 \times 10^6$ /m.

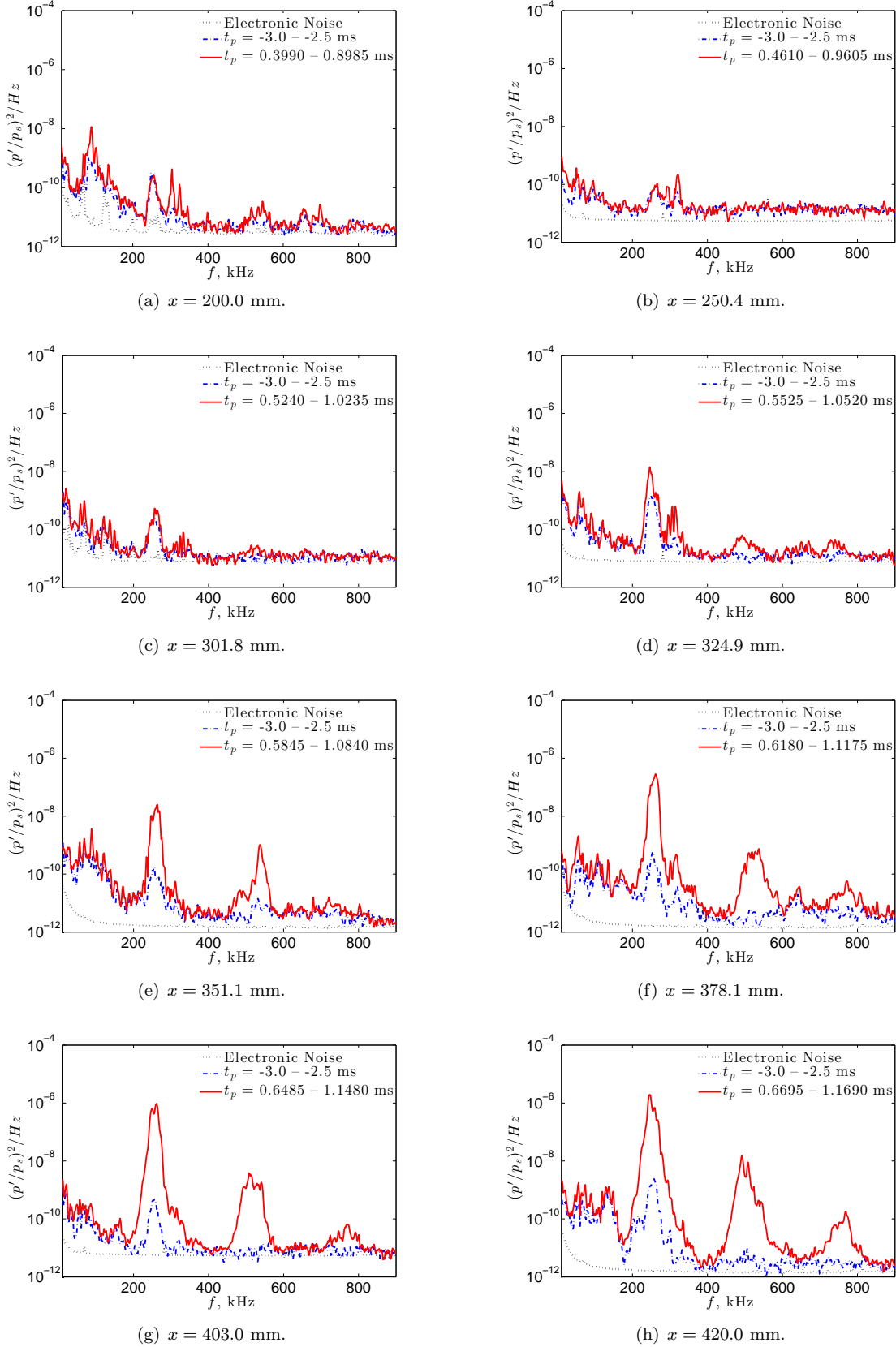


Figure 12. Power spectra showing the axial development of a laser-generated wave packet in the boundary layer of a blunt flared cone: $r_n = 1$ mm, $p_0 = 769.1$ kPa, $T_0 = 433.7$ K, $\rho_\infty = 0.032$ kg/m³, $Re/m = 8.22 \times 10^6$ /m.

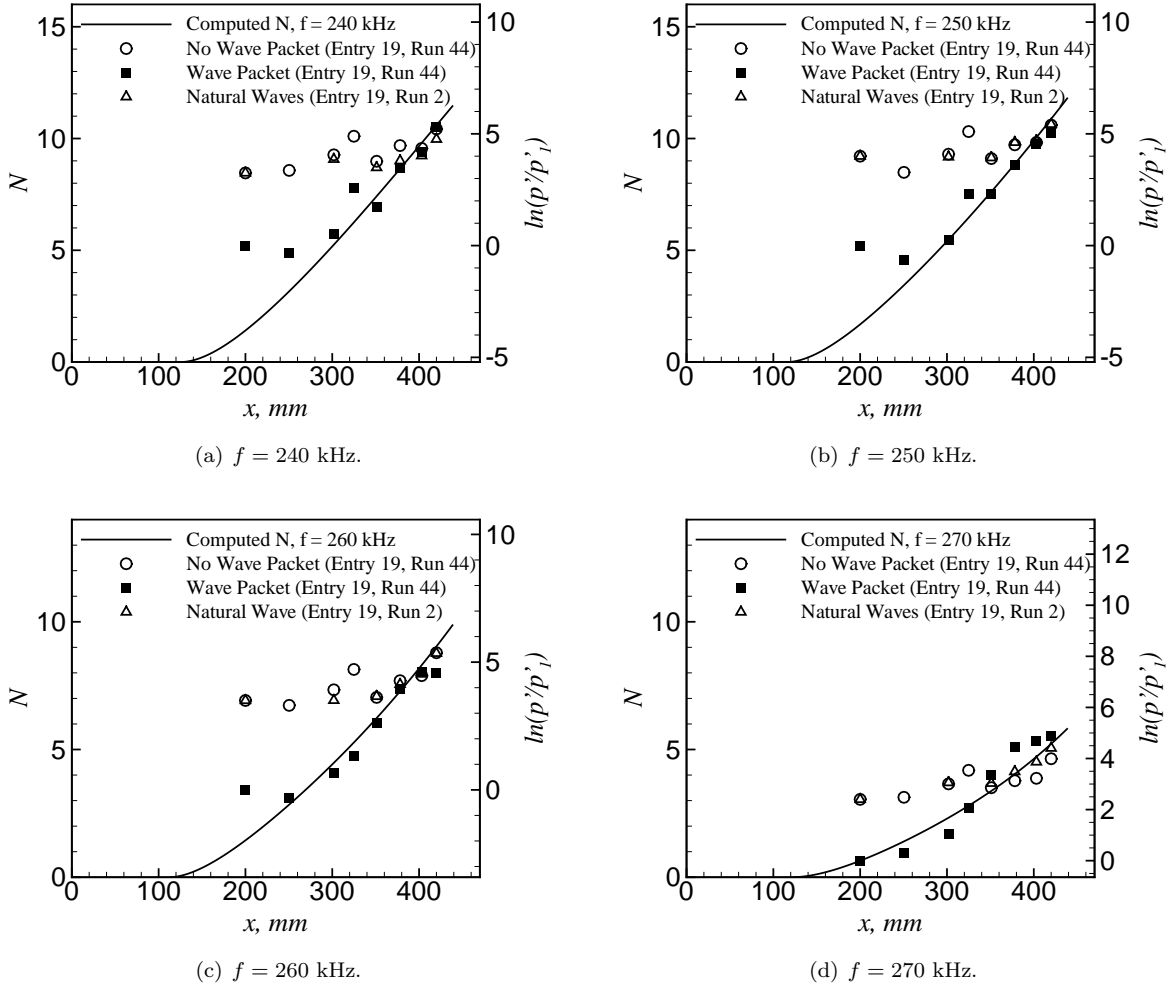


Figure 13. Comparison of normalized measured RMS at each sensor station on the blunt flared cone to the computed N factor: $r_n = 1$ mm, $p_0 = 769.1$ kPa, $T_0 = 433.7$ K, $\rho_\infty = 0.032$ kg/m³, $Re/m = 8.22 \times 10^6$ /m.

Table 2. Table of measured RMS amplitudes of the second-mode frequency peak on a blunt flared cone.

Axial Position x , mm	Normalized RMS	
	Pressure p'/p_s 150–350 kHz	Pressure p'/p_∞ 150–350 kHz
200.0	0.343	0.0403
250.4	0.294	0.0389
301.8	0.409	0.0609
324.9	1.29	0.203
351.1	2.52	0.421
378.1	8.70	1.55
403.0	15.0	2.83
420.0	16.2	3.18

each sensor station more clearly than the STFTs. These wavelet transforms are applied to the measurements on the blunt flared cone and shown in Fig. 14. The wavelet transform of the measurements at $x = 200$ mm shows that there is an increase in the wavelet transform magnitude at lower frequencies around 100 kHz. The lower frequency disturbance is not present for the next three sensor stations, but is present at $x = 351.1$ mm and $x = 420.0$ mm. A comparison of the power spectra in Fig. 12 indicates that this low-frequency peak is also present prior to the firing of a laser pulse, so it is likely unrelated to the presence of the wave packet. The increased amplitude at $t_p \approx 0.85$ ms is still seen in the wavelet transforms, but it is easier to distinguish between the presence of a wave packet in the aft sensors and the increase in noise. The double- and triple-burst wave packet structures are also evident in the wavelet transforms of the measurements at the most aft sensor stations.

VII. Summary and Conclusions

A freestream laser perturbation was used to generate a wave packet in the boundary layer on a flared cone. An analysis of the power spectra as it changes over time shows that the wave packet temporarily increases the amplitude of the boundary-layer instabilities. A peak is seen in the power spectra at a frequency that is within the range of a first-mode instability. However, the power in this peak is fairly similar before and after the arrival of the wave packet, and thus is unlikely to be related to the presence of the wave packet. Furthermore, this peak is only present at the first sensor station, and does not appear to grow with an increase in axial sensor station. The power in the second mode and its harmonics increases during the passage of the wave packet. On both the sharp and blunt flared cone, the presence of higher harmonics does not appear in the power spectra unless the wave packet is present. At the most aft measurement stations on the sharp flared cone, a broadband increase in the frequency content occurs during the passage of the wave packet, indicating breakdown of the wave packet. After the passage of the wave packet, the spectra show only the presence of a second-mode peak. This indicates that the effect of the large freestream laser perturbation temporarily causes breakdown to occur on the cone when the natural disturbances would otherwise not.

Some further investigation is required to determine the causes of some of the phenomena observed in the time-frequency analyses. First, at the farthest upstream measurement station, the wave packet contains a low-frequency peak, which does not appear to be related to the wave packet. However, computations by Huang et al.⁷ indicate that low-frequency waves arrive prior to the wave packet generated by a very small discrete thermal disturbance. While there is a slight increase in the lower-frequency peak when the wave packet in the current experiment passes by a sensor, the time-frequency analysis do not clearly indicate that this is the case. Second, on the blunt flared cone, an increase in power occurs at the second-mode frequency and its first harmonic. This increase in power does not appear to be convective because it appears on several sensors at the same time. Furthermore, this increase in power eventually abates because it does not appear just before the next laser pulse is fired. The cause of this increase is unknown. The unanswered questions and potential for future refinement of this experiment provide many opportunities for research.

Acknowledgments

This research was funded by AFOSR Grant FA9550-12-1-0167 and the NASA Pathways Intern Employment Program. Special thanks are given here to Professor Steven H. Collicott for designing the laser perturbation-generating optical system and to Dr. Bradley M. Wheaton and Dr. Thomas J. Juliano for the initial design of the flared cone model. Professor Rolf Radespiel is acknowledged here for suggesting the use of an offset perturbation for these studies. Dr. Michael Kegerise is acknowledged here for his guidance on time-frequency analyses. Dr. P. Balakumaris acknowledged for providing stability computations at the relevant conditions.

References

- ¹Morkovin, M. V., "Critical Evaluation of Transition from Laminar to Turbulent Shear Layers with Emphasis on Hypersonically Traveling Bodies," Tech. rep., Air Force Flight Dynamics Laboratory, Wright-Patterson Air Force Base, OH, Mar 1969, Technical Report AFFDL-TR-68-149.
- ²Marineau, E. C., Moraru, C. G., Lewis, D. R., Norris, J. D., Lafferty, J. F., Wagnild, R. M., and Smith, J. A., "Mach 10 Boundary-Layer Transition Experiments on Sharp and Blunted Cones," AIAA Paper 2014-3108, Jun 2014.
- ³Marineau, E. C., Moraru, C. G., Lewis, D. R., Norris, J. D., Lafferty, J. F., and Johnson, H. B., "Investigation of Mach

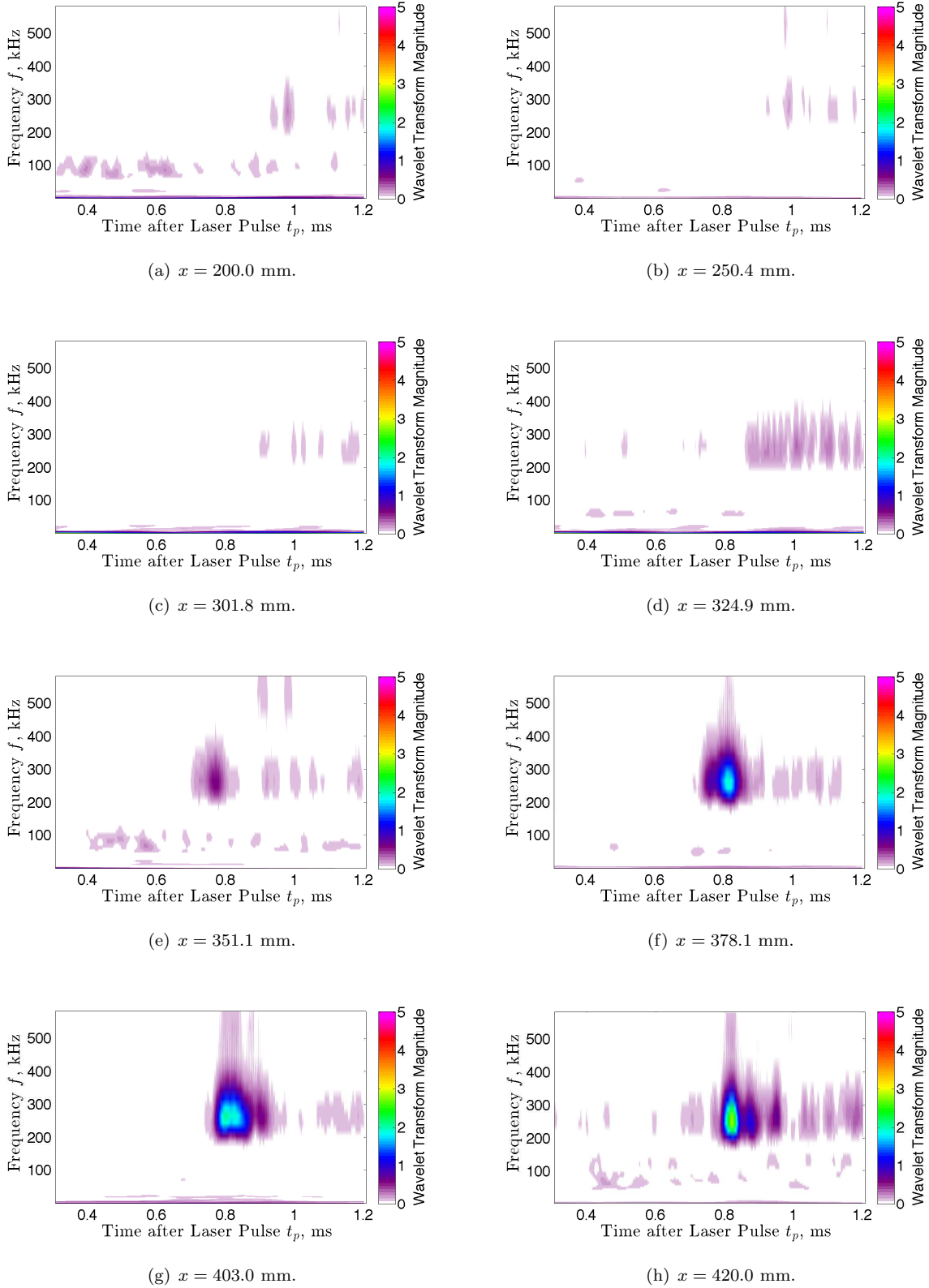


Figure 14. Morlet wavelet transforms showing the axial development of a laser-generated wave packet in the boundary layer of a blunt flared cone: $r_n = 1$ mm, $p_0 = 769.1$ kPa, $T_0 = 428.3$ K, $\rho_\infty = 0.032$ kg/m³, $Re/m = 8.22 \times 10^6$ /m.

10 Boundary Layer Stability of Sharp Cones at Angle-of-Attack, Part 1: Experiments," AIAA Paper 2015-1737, Jan 2015.

⁴Balakumar, P., "Receptivity of a Supersonic Boundary Layer to Acoustic Disturbances," *AIAA Journal*, Vol. 47, No. 5, May 2009, pp. 1069–1078.

⁵Balakumar, P. and Kegerise, M. A., "Receptivity of Hypersonic Boundary Layers over Straight and Flared Cones," AIAA Paper 2010-1065, Jan 2010.

⁶Balakumar, P. and Kegerise, M. A., "Receptivity of Hypersonic Boundary Layers to Acoustic and Vortical Disturbances," AIAA Paper 2011-0371, Jan 2011.

⁷Huang, Y. and Zhong, X., "Parametric Study of Boundary-Layer Receptivity to Freestream Hot-Spot Perturbation over a Blunt Compression Cone," AIAA Paper 2014-774, Jan 2014.

⁸Fedorov, A. V., Ryzhov, A. A., and Soudakov, V. G., "Numerical and theoretical modeling of supersonic boundary-layer receptivity to temperature spottiness," AIAA Paper 2011-3077, Jun 2011.

⁹Fedorov, A. V. and Kozlov, M. V., "Receptivity of high-speed boundary layer to solid particulates," AIAA Paper 2011-3925, Jun 2011.

¹⁰Maslov, A. A., Shiplyuk, A. N., Sidorenko, A. A., and Arnal, D., "Leading-edge receptivity of a hypersonic boundary layer on a flat plate," *Journal of Fluid Mechanics*, Vol. 426, 2001, pp. 73–94.

¹¹Schmisser, J. D., Collicott, S. H., and Schneider, S. P., "Laser-Generated Localized Freestream Perturbations in Supersonic and Hypersonic Flows," *AIAA Journal*, Vol. 38, No. 4, Apr 2000, pp. 666–671.

¹²Heitmann, D. and Radespiel, R., "Simulations of Boundary-Layer Response to Laser-Generated Disturbances at Mach 6," *Journal of Spacecraft and Rockets*, Vol. 50, No. 2, Mar–Apr 2013, pp. 305–316.

¹³Huang, Y. and Zhong, X., "Numerical Study of Hypersonic Boundary-Layer Receptivity with Freestream Hotspot Perturbations," *AIAA Journal*, Vol. 52, No. 12, Dec 2014, pp. 2652–2672.

¹⁴Salyer, T. R., Collicott, S. H., and Schneider, S. P., "Characterizing Laser-Generated Hot Spots for Receptivity Studies," *AIAA Journal*, Vol. 44, No. 12, Dec 2006, pp. 2871–2878.

¹⁵Chou, A., *Mach-6 Receptivity Measurements of Laser-Generated Perturbations on a Flared Cone*, Ph.D. thesis, School of Aeronautics & Astronautics, Purdue University, West Lafayette, IN, Aug 2014.

¹⁶Chou, A., Schneider, S. P., and Kegerise, M. A., "Characterization of a Laser-Generated Perturbation in High-Speed Flow for Receptivity Studies," AIAA Paper 2014-0773, Jan 2014.

¹⁷Chou, A., Schneider, S. P., and Collicott, S. H., "Boundary Layer Instabilities Generated by Freestream Laser Perturbations," AIAA Paper 2015-1734, January 2015.

¹⁸Steen, L. E., *Characterization and Development of Nozzles for a Hypersonic Quiet Wind Tunnel*, Master's thesis, School of Aeronautics & Astronautics, Purdue University, West Lafayette, IN, Dec 2010.

¹⁹Wheaton, B. M., Juliano, T. J., Berridge, D. C., Chou, A., Gilbert, P. L., Casper, K. M., Steen, L. E., Schneider, S. P., and Johnson, H. B., "Instability and Transition Measurements in the Mach-6 Quiet Tunnel," AIAA Paper 2009-3559, Jun 2009.

²⁰Berridge, D. C., Chou, A., Ward, C. A., Steen, L. E., Gilbert, P. L., Juliano, T. J., Schneider, S. P., and Gronvall, J. E., "Hypersonic Boundary-Layer Transition Experiments in a Mach-6 Quiet Tunnel," AIAA Paper 2010-1061, Jan 2010.

²¹Balakumar, P. and Reed, H. L., "Stability of three-dimensional supersonic boundary layers," *Physics of Fluids*, Vol. 3, No. 4, Apr 1991, pp. 617–632.

²²Jordan, D., Miksad, R. W., and Powers, E. J., "Implementation of the continuous wavelet transform for digital time series analysis," *Review of Scientific Instruments*, Vol. 68, No. 3, Mar 1997, pp. 1484–1494.

²³Sivasubramanian, J. and Fasel, H. F., "Growth and Breakdown of a Wave Packet into a Turbulent Spot in a Cone Boundary Layer at Mach 6," AIAA Paper 2012-0085, Jan 2012.

²⁴Terwilliger, N., *Numerical Investigation of Boundary Layer Instability Modes on a Compression Cone at Mach 6*, Master's thesis, Department of Aerospace and Mechanical Engineering, The University of Arizona, 2011.